Draft version June 14, 2023
Typeset using LaTeX default style in AASTeX631

Scattering of ions at a rippled shock

Michael Gedalin [1], Nikolai V. Pogorelov [2,3] and Vadim Roytershteyn [4]

[1] Department of Physics, Ben Gurion University of the Negev, Beer-Sheva, Israel
[2] Department of Space Science, The University of Alabama in Huntsville, AL 35805, USA
[3] Center for Space Plasma and Aeronomic Research, The University of Alabama in Huntsville, AL 35805, USA
[4] Space Science Institute, Boulder, CO 80301, USA

(Received; Revised; Accepted)

ABSTRACT

In a collisionless shock the energy of the directed flow is converted to heating and acceleration of charged particles, and to magnetic compression. In low-Mach number shocks the downstream ion distribution is made of directly transmitted ions. In higher-Mach number shocks ion reflection is important. With the increase of the Mach number rippling develops which is expected to affect ion dynamics. Using ion tracing in a model shock front, downstream distributions of ions are analyzed and compared for a planar stationary shock with an overshoot and a similar shock with ripples propagating along the shock front. It is shown that rippling results in the distributions which are substantially broader and more diffuse in the phase space. Gyrotropization is sped up. Rippling is able to generate backstreaming ions which are absent in the planar stationary case.

Keywords: shock waves – acceleration of particles

1. INTRODUCTION

Collisionless shocks are one of the most ubiquitous phenomena in space plasmas (see Treumann 2009, for a review and further references). At a fast magnetosonic shock the energy of the directed plasma flow is re-distributed. A large part of it is converted into ion heating. At low Mach numbers, ion heating is due to the gyration of the directly transmitted ions (Gedalin 1997, 2021). The corresponding post-shock (downstream) distributions are initially non-gyrotropic and gradually gyrotropize and isotropize (Gedalin et al. 2015b). At sufficiently high Mach numbers, ion reflection becomes important. Reflected ions contribute substantially to the downstream ion temperature (Phillips & Robson 1972; Gosling et al. 1982; Sckopke et al. 1983, 1990). Ion reflection is affected by the shock structure, in particular, by the overshoot (Gedalin et al. 2023). With the increase of the Mach number, the shock front undergoes structural changes, like rippling (Lowe & Burgess 2003; Moullard et al. 2006; Lobzin et al. 2008; Yang et al. 2012; Ofman & Gedalin 2013; Johlander et al. 2016; Gingell et al. 2017; Johlander et al. 2018; Hanson et al. 2019; Omidi et al. 2021). Rippling causes deviations of the local normal to the shock transition layer from the global normal determined by the conservation laws, a.k.a., Rankine-Hugoniot relations (Ofman & Gedalin 2013). Therefore, the dynamics of ions, entering the shock at different spatial locations, is affected by different fields, and the downstream distributions near the shock front, produced at different sites. Further downstream these distributions mix to evolve into a single uniform gyrotropic distribution. The relation of the uniform upstream ion distribution to the far downstream gyrotropic distribution can be described as scattering at the shock front (Gedalin et al. 2015a). The exact influence of the shock rippling on the ion scattering is not known at present. Observations provide detailed information on ion distributions along the spacecraft trajectory. Multi-spacecraft observations may provide distributions simultaneously along several close spacecraft paths. Self-consistent numerical simulations may provide detailed distributions in two or even three dimensions. However, neither observations, nor simulations are capable of separating the effects of rippling, since it is

Corresponding author: Michael Gedalin
gedalin@bgu.ac.il

not possible to make observations or perform simulations for the same shock parameters with ripples being eliminated. Here a test particle analysis may be useful. The idea is to determine the ion distributions formed in a stationary plane shock model and compare these distributions with those obtained in the same profile with rippling added.

2. A MODEL SHOCK PROFILE

The stationary plane model used in the analysis is based on the following profile:

$$B_x = \cos\theta_{Bn} \tag{1}$$

$$B_z = B\sin\theta_{Bn} \tag{2}$$

$$B_y = k_B\left(\frac{dB}{dx}\right) \tag{3}$$

$$E_x = -k_E\left(\frac{dB}{dx}\right) \tag{4}$$

$$E_y = \sin\theta_{Bn} \tag{5}$$

$$E_z = 0 \tag{6}$$

$$B = B_{bas} + B_{add} \tag{7}$$

$$B_{bas} = \frac{R_{bas}-1}{2} + \frac{R_{bas}+1}{2}\tanh\frac{3x}{D} \tag{8}$$

$$B_{add} = R_{add}\left(1-\tanh\frac{3(x-c_r)}{w_r}\right)\left(1+\tanh\frac{3(x-c_l)}{w_l}\right) \tag{9}$$

Here the magnetic field is normalized on the upstream magnetic field B_u and the electric field is normalized on V_uB_u/c. The coefficients k_E and k_B are determined by the cross-shock potential (see below). The coordinate x and all lengths are normalized on the upstream convective gyroradius, V_u/Ω_u, where V_u is the plasma speed in the normal incidence frame (NIF) and $\Omega_u = eB_u/m_pc$ is the upstream proton, p, gyrofrequency. NIF is the shock frame in which the upstream plasma flow is directed along the shock normal. The upstream ion inertial length is c/ω_{pi}, where $\omega_{pi} = \sqrt{4\pi e^2 n_u/m_p}$ and n_u are the upstream proton plasma frequency and the upstream proton number density. The Alfvénic Mach number is $M_A = V_u/v_A$, where the Alfvén speed is $v_A = B_u/\sqrt{4\pi n_u m_p}$. We shall also use the angle θ_{Bn} between the shock normal and the upstream magnetic field vector. The magnetic compression is

$$\frac{B_d}{B_u} = \sqrt{\cos^2\theta_{Bn} + R_{bas}^2\sin^2\theta_{Bn}} \tag{10}$$

The expression Eq. (8) describes a monotonic transition from the upstream magnetic field to the downstream magnetic field (the main varying component). Eq. (9) adds an overshoot. Eq. (3) describes the noncoplanar magnetic field which is nonzero only inside the transition layer. The motional electric field (5) is constant throughout the shock. The cross-shock electric field along the shock normal (4) is also present only inside the transition layer. In a planar stationary shock E_z is identically zero. The coefficients k_E and k_B are determined by the cross-shock potential:

$$-\int E_x dx = \phi_{NIF} \equiv s_{NIF}(m_pV_u^2/2e) \tag{11}$$

$$-\int (E_x + V_u\tan\theta_{Bn}B_y/c)dx = \phi_{HT} \equiv s_{HT}(m_pV_u^2/2e) \tag{12}$$

The subscript HT means de Hoffman-Teller frame. The latter is the shock frame in which the upstream plasma flow is along the upstream magnetic field. The parameters θ_{Bn}, B_d/B_u, R_{add}, s_{NIF}, s_{HT}, D, c_l, c_r, w_l, w_r, k_E, and k_B completely define the adopted model of a planar stationary shock profile.

Rippling is added by the replacement

$$x \to X = x - a\psi g \tag{13}$$

$$\psi(y,z,t) = \sin(k_{rip}(z\cos\varphi + y\sin\varphi - V_{rip}t)) \tag{14}$$

$$g(x) = \left(1+\tanh\frac{3(x-X_L)}{W_L}\right)\left(1-\tanh\frac{3(x-X_R)}{W_R}\right) \tag{15}$$

in NIF. Accordingly, $B(x) \to B(X)$, and

$$B_x = k_B \left(\frac{dB}{dX}\right)\left(\frac{\partial X}{\partial y}\right) - B\sin\theta_{Bn}\left(\frac{\partial X}{\partial z}\right) + \cos\theta_{Bn} \tag{16}$$

$$B_y = -k_B \left(\frac{dB}{dX}\right)\left(\frac{\partial X}{\partial x}\right) \tag{17}$$

$$B_z = B\sin\theta_{Bn}\left(\frac{\partial X}{\partial x}\right) \tag{18}$$

$$E_x = -k_E \left(\frac{dB}{dX}\right)\left(\frac{\partial X}{\partial x}\right) \tag{19}$$

$$E_y = \sin\theta_{Bn} - B\sin\theta_{Bn}\left(\frac{\partial X}{\partial t}\right) - k_E\left(\frac{dB}{dX}\right)\left(\frac{\partial X}{\partial y}\right) \tag{20}$$

$$E_z = -k_B \left(\frac{dB}{dX}\right)\left(\frac{\partial X}{\partial t}\right) - k_E\left(\frac{dB}{dX}\right)\left(\frac{\partial X}{\partial z}\right) \tag{21}$$

These fields are the fields in NIF. The ripples are moving along the shock front with the velocity $\boldsymbol{V}_{rip} = V_{rip}(0, \sin\varphi, \cos\varphi)$. In the rippling frame the fields become time independent. The speed V_{rip} is of the order of the Alfvén speed (Johlander et al. 2016; Gingell et al. 2017; Johlander et al. 2018; Omidi et al. 2021) and we may apply the nonrelativistic transformation

$$E'_x = E_x + V_{rip}\sin\varphi B_z - V_{rip}\cos\varphi B_y \tag{22}$$

$$E'_y = E_y + V_{rip}\cos\varphi B_x \tag{23}$$

$$E'_z = E_z - V_{rip}\sin\varphi B_x \tag{24}$$

The advantage of the rippling frame for ion tracing is that it is not necessary to take into account time dependence. The two-dimensional surface of the magnetic field magnitude for the rippled shock is shown in Figure 1. The rippling

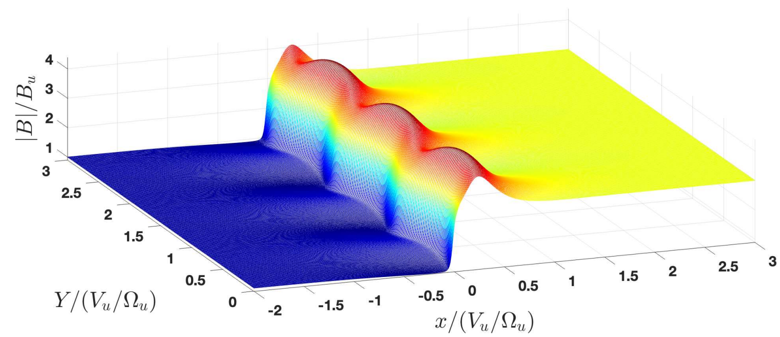

Figure 1. The two-dimensional surface of the magnetic field magnitude for the rippled shock. Y is in the direction or rippling propagation. The global shock normal is along x. The local shock normal is determined by the steepest gradient of the magnetic field magnitude, depends on Y, and differs from the global normal. The maximum overshoot magnetic field also depends on Y.

is localized around the shock transition and disappears sufficiently far upstream and downstream.

3. PRINCIPLES OF TEST PARTICLE ANALYSIS

An incident ion distribution is specified and for each ion the equations of motion in the corresponding dimensionless form

$$\frac{d\boldsymbol{r}}{dt} = \boldsymbol{v}, \quad \frac{d\boldsymbol{v}}{dt} = \boldsymbol{E} + \boldsymbol{v}\times\boldsymbol{B} \tag{25}$$

are solved numerically. Here the velocity $\boldsymbol{v}$ is normalized on V_u, the position vector $\boldsymbol{r}$ is normalized on V_u/Ω_u, and time is normalized on Ω_u^{-1}. The distribution function $f(\boldsymbol{v}, \boldsymbol{r}, t)$ throughout the shock front is derived using $df/dt = 0$

along the particle trajectory, that is, $f(\boldsymbol{v}, \boldsymbol{r}, t) = f(\boldsymbol{v}_0, \boldsymbol{r}_0, t_0)$, where

$$\boldsymbol{r} = \boldsymbol{r}(t; \boldsymbol{v}_0, \boldsymbol{r}_0, t_0), \quad \boldsymbol{v} = \boldsymbol{v}(t; \boldsymbol{v}_0, \boldsymbol{r}_0, t_0) \tag{26}$$

is the solution of the equations of motion with the initial conditions

$$\boldsymbol{r}(t = t_0) = \boldsymbol{r}_0, \quad \boldsymbol{v}(t = t_0) = \boldsymbol{v}_0 \tag{27}$$

For the stationary plane shock ion tracing is done in NIF, where the fields depend only on x, we have $f = f(x, \boldsymbol{v})$. For the rippled shock ion tracing is done in the rippling frame, where the fields are time independent, $f = f(x, y, z, \boldsymbol{v})$. The moments of the distribution function are derived as follows:

$$\int \psi(x, y, z, \boldsymbol{v}) f(x, y, z, \boldsymbol{v}) d^3\boldsymbol{v} = \int \psi f(x_0, y_0, z_0, \boldsymbol{v}_0) |J| d^3\boldsymbol{v}_0 \tag{28}$$

where the Jacobian is

$$J = \det\left(\frac{\partial v_i(x, y, z)}{\partial v_j(0)}\right) = \frac{v_{0x}}{v_x}, \quad i, j = x, y, z \tag{29}$$

(see Appendix). In Eqs. (28) and (29) the velocity $\boldsymbol{v}$ depends on the initial conditions and on the current position. Note that for ion tracing in the rippled shock the initial velocity distribution should be shifted $\boldsymbol{v}_0 \to \boldsymbol{v}_0 - \boldsymbol{V}_{rip}$. In the whole analysis all velocities are normalized on V_u.

4. DISTRIBUTIONS

In the present analysis the following parameters were used: $M_A = 6$, $\theta_{Bn} = 60°$, $\beta_i = 1$, $B_d/B_u = 3$, $B_{add} = 1$, $s_{NIF} = 0.4$, $s_{HT} = 0.1$, $D = 2/M$, $k_{rip} = 2\pi$, $\varphi = 45°$, $V_{rip} = 1/M$, $w_l = D$, $w_r = 3D$, $x_l = 0.5D$, $x_r = 0.5D$, $W_L = 2$, $W_R = 2$, $X_L = 0$, $X_R = 0$. The incident ion distribution is Maxwellian with $\beta_i = 8\pi n_u T_{iu}/B_u^2 = 1$.

In the shock without rippling it is sufficient to start tracing at the same (x_0, y_0, z_0). Figure 2 shows the reduced distribution functions $f(x, v_x)$, $f(x, v_y)$, and $f(x, v_z)$, for the case without rippling. Each reduced distribution function is obtained by integration over two other components of the velocity, e.g.,

$$f(x, v_x) = \int f(x, \boldsymbol{v}) dv_y dv_z \tag{30}$$

The distribution functions are shown on the log scale. The top panel shows $f(x, v_x)$, the middle panel shows $f(x, v_y)$, and the bottom panel is for $f(x, v_z)$. The black line in each panel shows the magnetic field magnitude. Various populations in the ion distribution marked on the top panel. The directly transmitted ions and the reflected-transmitted ions (ions which cross the shock again after reflection) are clearly seen. There are well pronounced dips (ion phase space holes) in the distribution function. Non-gyrotropy of the downstream distribution is quite clear. Relaxation to gyrotropy is gradual but rather fast, because of the overshoot (Gedalin et al. 2023).

The ultimate objective of the test particle analysis is the determination of the downstream gyrotropic function $f_d(v_\parallel, v_\perp)$ sufficiently far from the shock transition layer. Here $\parallel$ and $\perp$ refer to the direction of the downstream magnetic field, and the distribution function is calculated in HT. The same Jacobian as in Eq. (29) is added as a weight in the calculation of the distribution function. Figure 3 shows the gyrotropic distribution of incident ions in the upstream region on the log scale. Figure 4 shows the gyrotropic distribution of the downstream ions. The distribution consists of two distinct populations: the directly transmitted ions and the reflected-transmitted ions. Both populations have rather smooth shapes possessing maxima and monotonic decrease around them.

For the rippled shock the incident ions start at the same x_0 but their positions along the rippling direction are chosen randomly within the rippling wavelength $2\pi/k_{rip}$. Figure 5 shows the reduced distribution functions $f(x, v_x)$, $f(x, v_y)$, and $f(x, v_z)$, for the case with rippling. The distribution functions are integrated over the coordinates perpendicular to the shock normal direction. The magnetic field is represented not by a line but by a ribbon, because each ion is measuring its own magnetic field magnitude along its trajectory. The integrated distribution of the directly transmitted ions is nearly gyrotropic because of the mixing of ions appearing at the same cross-section $x = \text{const}$ but at different y and z. In all three panels the backstreaming ions are clearly seen. In the top panel these ions have $v_x < 0$ farther from the shock than the turning distances of the reflected ions which later cross the shock again. In the bottom panel these backstreaming ions all have $v_z < -2$ and are completely separated from other populations.

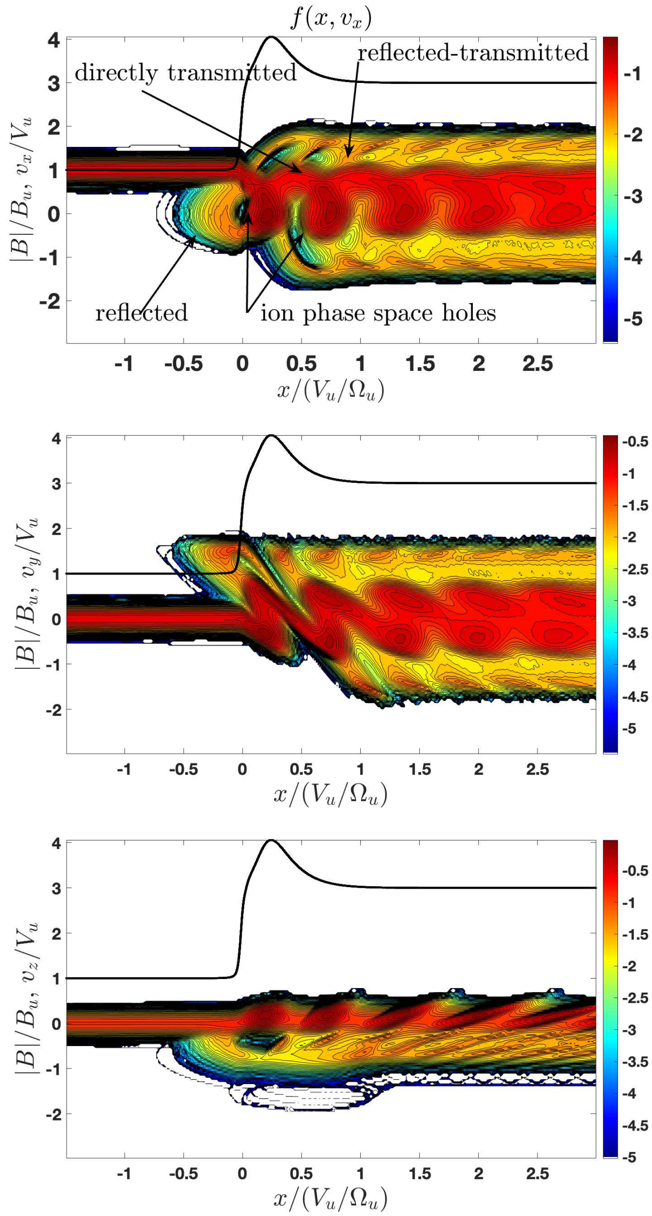

Figure 2. Reduced distribution functions for the case without rippling. Top: $f(x, v_x)$. Middle: $f(x, v_y)$. Bottom: $f(x, v_z)$. The black line shows the magnetic field magnitude. All distinct ion populations are indicated on the top panel: a) the directly transmitted ions cross the shock and proceed further downstream, b) the reflected ions are seen just ahead of the shock transition, c) the reflected-transmitted ions are the reflected ions which cross the shock again and proceed further downstream. Ion phase space holes are the regions where the phase space density is very low and even approaches zero. Non-gyrotropy of the downstream distribution persists well into the downstream region.

The downstream gyrotropic distribution is derived in the region where rippling is no longer noticeable, and is also done in HT. It is shown in Figure 6. The directly transmitted and reflected-transmitted populations are still clearly separated but both are very diffuse and not smooth. The distribution of reflected-transmitted ions is especially broad.

Figure 7 shows the gyrotropic distribution function of backstreaming ions far upstream of the shock. The number of these ions is low. The distribution is rather diffuse with substantial $v_\perp$ for most ions, so that the pitch-angle ψ, $\cos\psi = |v_\parallel|/\sqrt{v_\parallel^2 + v_\perp^2}$ is large.

5. CONCLUSIONS

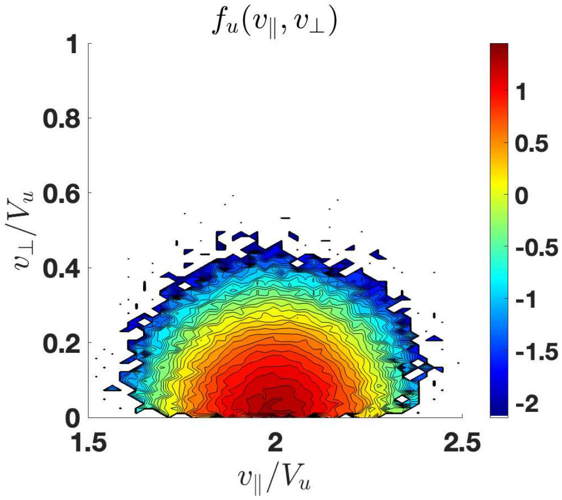

Figure 3. Gyrotropic distribution function of incident ions. The distribution is Maxwellian with the normalized thermal speed $v_T \approx 0.11$.

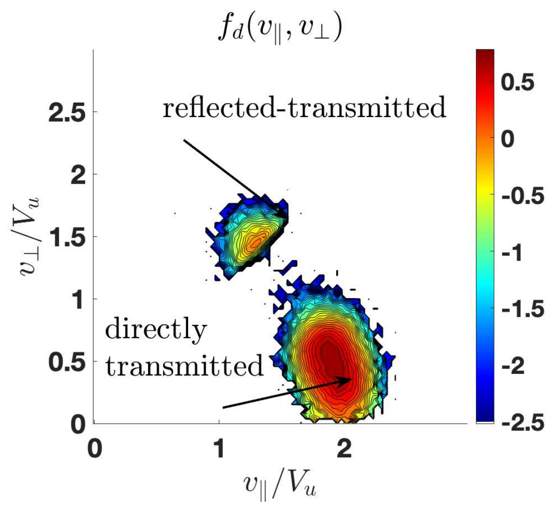

Figure 4. Downstream gyrotropic distribution function in the shock without rippling. The downstream populations of the directly transmitted ions and the reflected-transmitted ions are clearly distinct.

Rippling significantly changes ion scattering at the shock front. Integrated downstream distributions are nearly gyrotropic in the rippled case while non-gyrotropy is prominent in the stationary planar counterpart. Far downstream the gyrotropic distributions are much broader and much more diffuse in the phase space. Rippling produces backstreaming ions which are absent without rippling. Thus, rippling may be a clue to the solution of the injection problem: generation of a population of superthermal ions escaping to the upstream region from the shock. These ions can be further accelerated to higher energies by the diffusive shock acceleration mechanism (Giacalone 2003). Previous studies of planar stationary shocks have not found backstreaming ions for $\theta_{Bn} > 50^\circ$ (Gedalin et al. 2008), while observations have shown their presence at quasi-perpendicular shocks (Kucharek et al. 2004). Local normals in a rippled shock are different at different positions and different from the global normal (Ofman & Gedalin 2013). This may be the main reason of the changes in ion reflection causing production of backstreaming ions at even a globally quasi-perpendicular shock.

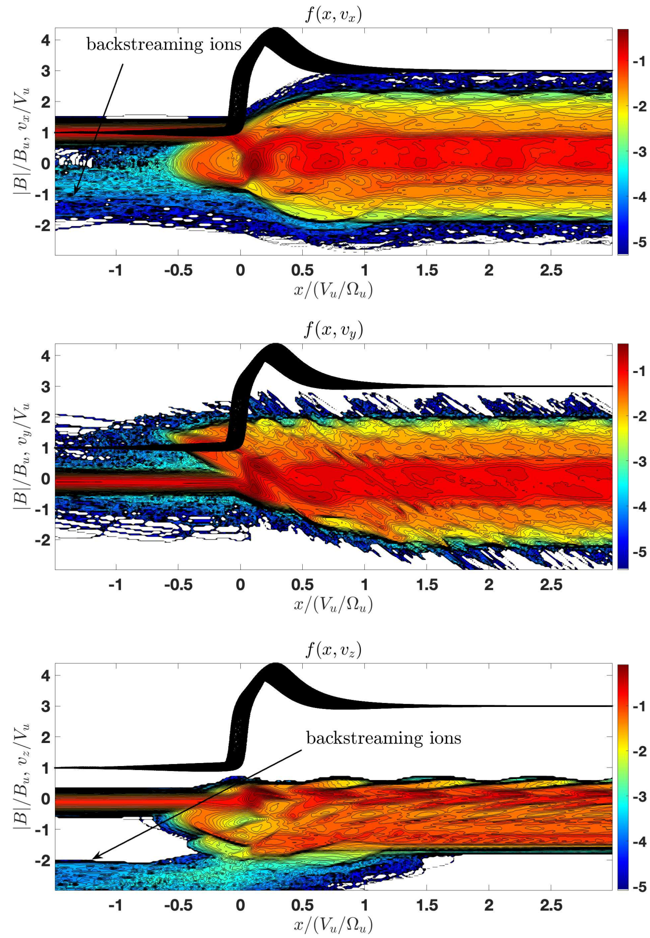

Figure 5. Reduced distribution functions for the case with rippling. Top: $f(x, v_x)$. Middle: $f(x, v_y)$. Bottom: $f(x, v_z)$. The black ribbon shows the magnetic field magnitude as observed by ions crossing the shock in different positions. The directly transmitted, reflected, and reflected-transmitted ions are clearly seen but ion phase space holes are filled with ions. Gyrotropization of the downstream distribution occurs within one ion convective gyroradius. The most important change is the appearance of the backstreaming ions.

M. Gedalin was partially supported by NSF-BSF grant 2019744 and by the European Union's Horizon 2020 research and innovation program under grant agreement No 101004131 (SHARP). N. Pogorelov was supported, in part, by NSF-BSF award 2010450 and NASA grant 80NSSC18K1649. NP was additionally supported by the *IBEX* mission as a part of NASA's Explorer program. V. Roytershteyn was partially supported by NASA grant 80NSSC18K1649 and NSF-BSF award 2010144. Resources supporting this work were provided by the NASA High-End Computing (HEC) Program through the NASA Advanced Supercomputing (NAS) Division at Ames Research Center.

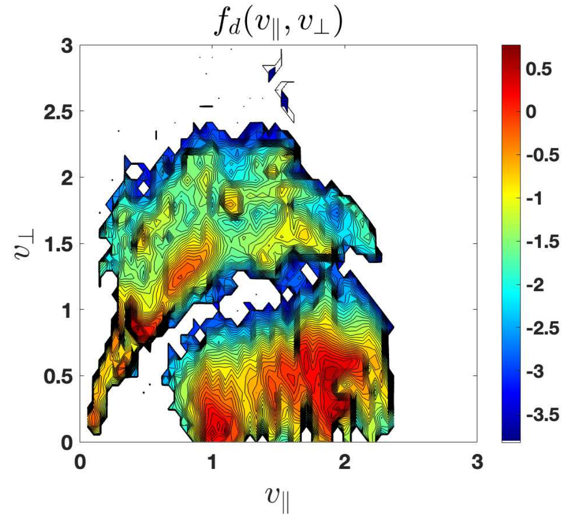

Figure 6. Downstream gyrotropic distribution function in the rippled shock. Compare with Figure 4. Both directly transmitted and reflected-transmitted populations are more diffuse since they consist of particles coming from different crossing positions.

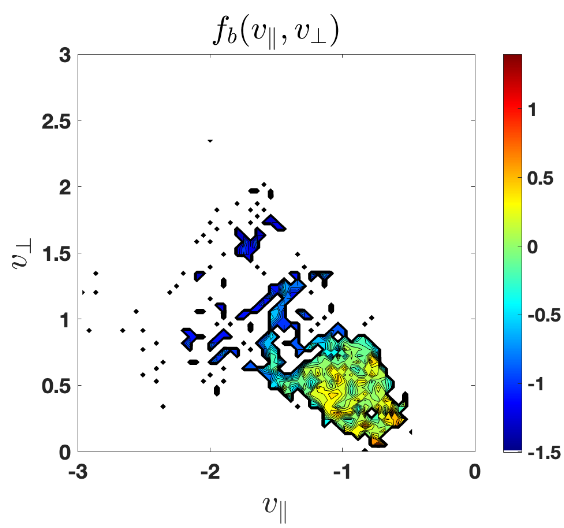

Figure 7. Gyrotropic distribution function of backstreaming ions in the rippled shock. The distribution is rather broad. There is substantial dispersion in $v_\parallel$ and $v_\perp$.

APPENDIX

A. JACOBIAN DERIVATION

We consider electric and magnetic fields which depend on (x, y, z), while the plasma flow is along x. For simplicity we limit ourselves with the non-relativistic case. Relativistic generalization is straightforward. Given $\boldsymbol{r}_0$ the velocity of the particle depends on $\boldsymbol{r}$. This function $\boldsymbol{v}(\boldsymbol{r})$ may be not single-valued but otherwise is time-independent. The Jacobian

$$J(\boldsymbol{r}) = \det\left(\frac{\partial v_i(\boldsymbol{r})}{\partial u_j(0)}\right) \tag{A1}$$

will be time-independent too. Let us consider

$$J(\boldsymbol{r}+d\boldsymbol{r}) = J(\boldsymbol{r}) + dJ \tag{A2}$$

$$dJ = \boldsymbol{\nabla} J \cdot d\boldsymbol{r} \tag{A3}$$

$$J(\boldsymbol{r}+d\boldsymbol{r}) = J(\boldsymbol{r})\det\left(\frac{\partial v_i(\boldsymbol{r}+d\boldsymbol{r})}{\partial v_j(\boldsymbol{r})}\right) \tag{A4}$$

$$J(\boldsymbol{r}+d\boldsymbol{r}) = J(\boldsymbol{r})\left(1 + \mathrm{Tr}\left(\frac{\partial dv_i}{\partial v_j}\right)\right) \tag{A5}$$

$$d\boldsymbol{v} = \boldsymbol{g}dt \tag{A6}$$

$$\boldsymbol{g} = \frac{q}{m}(\boldsymbol{E} + \boldsymbol{v}\times\boldsymbol{B}) \tag{A7}$$

We have

$$dt = \frac{dx}{v_x}, \quad dy = \frac{v_y dx}{v_x}, \quad dz = \frac{v_z dx}{v_x} \tag{A8}$$

$$dv_x = \frac{g_x dx}{v_x}, \quad dv_y = \frac{g_y dx}{v_x}, \quad dv_z = \frac{g_z dx}{v_x} \tag{A9}$$

For given dx

$$\frac{\partial dv_x}{\partial v_x} = \frac{\partial}{\partial v_x}\frac{g_x dx}{v_x} = -\frac{g_x dx}{v_x^2} = -\frac{dv_x}{v_x} \tag{A10}$$

$$\frac{\partial dv_y}{\partial v_y} = \frac{\partial}{\partial v_y}\frac{g_y dx}{v_x} = 0 \tag{A11}$$

$$\frac{\partial dv_z}{\partial v_z} = \frac{\partial}{\partial v_z}\frac{g_z dx}{v_x} = 0 \tag{A12}$$

therefore

$$dJ = -J\frac{dv_x}{v_x}, \quad J = \frac{v_{0x}}{v_x} \tag{A13}$$

Note that in this expression v_x depends on $\boldsymbol{v}_0$, $\boldsymbol{r}_0$, and $\boldsymbol{r}$.

REFERENCES

Gedalin, M. 1997, Geophys. Res. Lett., 24, 2511, doi: 10.1029/97GL02524

—. 2021, Astrophys. J., 912, 82, doi: 10.3847/1538-4357/abf1e2

Gedalin, M., Dimmock, A. P., Russell, C. T., Pogorelov, N. V., & Roytershteyn, 2023, J. Plasma Phys., 89, 905890201, doi: 10.1017/S0022377823000090

Gedalin, M., Dröge, W., & Kartavykh, Y. Y. 2015a, Astrophys. J., 807, 126, doi: 10.1088/0004-637X/807/2/126

Gedalin, M., Friedman, Y., & Balikhin, M. 2015b, Phys. Plasmas, 22, 072301, doi: 10.1063/1.4926452

Gedalin, M., Liverts, M., & Balikhin, M. A. 2008, J. Geophys. Res., 113, 05101, doi: 10.1029/2007JA012894

Giacalone, J. 2003, Plan. Sp. Sci., 51, 659, doi: 10.1016/S0032-0633(03)00101-6

Gingell, I., Schwartz, S. J., Burgess, D., et al. 2017, J. Geophys. Res, 77, 736, doi: 10.1002/2017JA024538

Gosling, J. T., Thomsen, M. F., Bame, S. J., et al. 1982, Geophys. Res. Lett., 9, 1333, doi: 10.1029/GL009i012p01333

Hanson, E. L. M., Agapitov, O. V., Mozer, F. S., et al. 2019, Geophys. Res. Lett., 46, 2381, doi: 10.1029/2018GL080240

Johlander, A., Vaivads, A., Khotyaintsev, Y. V., et al. 2018, Plasma Phys. Contr. Fus., 60, 125006, doi: 10.1088/1361-6587/aae920

Johlander, A., Schwartz, S. J., Vaivads, A., et al. 2016, Phys. Rev. Lett., 117, 165101, doi: 10.1103/PhysRevLett.117.165101

Kucharek, H., Möbius, E., Scholer, M., et al. 2004, Annales Geophysicae, 22, 2301, doi: 10.5194/angeo-22-2301-2004

Lobzin, V. V., Krasnoselskikh, V. V., Musatenko, K., & Dudok de Wit, T. 2008, Annales Geophysicae, 26, 2899, doi: 10.5194/angeo-26-2899-2008

Lowe, R. E., & Burgess, D. 2003, Annales Geophysicae, 21, 671, doi: 10.5194/angeo-21-671-2003

Moullard, O., Burgess, D., Horbury, T. S., & Lucek, E. A. 2006, J. Geophys. Res, 111, A09113, doi: 10.1029/2005JA011594

Ofman, L., & Gedalin, M. 2013, J. Geophys. Res, 118, 5999, doi: 10.1002/2013JA018780

Omidi, N., Desai, M., Russell, C. T., & Howes, G. G. 2021, J. Geophys. Res, 126, e2021JA029287, doi: 10.1029/2021JA029287

Phillips, P. E., & Robson, A. E. 1972, Phys. Rev. Lett., 29, 154, doi: 10.1103/PhysRevLett.29.154

Sckopke, N., Paschmann, G., Bame, S. J., Gosling, J. T., & Russell, C. T. 1983, J. Geophys. Res, 88, 6121, doi: 10.1029/JA088iA08p06121

Sckopke, N., Paschmann, G., Brinca, A. L., Carlson, C. W., & Luehr, H. 1990, J. Geophys. Res, 95, 6337, doi: 10.1029/JA095iA05p06337

Treumann, R. A. 2009, Astron. Astrophys. Rev., 17, 409, doi: 10.1007/s00159-009-0024-2

Yang, Z. W., Lembège, B., & Lu, Q. M. 2012, J. Geophys. Res, 117, A07222, doi: 10.1029/2011JA017211